NASA Technical Paper 1263

Jupiter Probe Charging Study

Carolyn K. Purvis

JANUARY 1979

NASA

NASA Technical Paper 1263

Jupiter Probe Charging Study

Carolyn K. Purvis
Lewis Research Center
Cleveland, Ohio

National Aeronautics
and Space Administration

**Scientific and Technical
Information Office**

1979

JUPITER PROBE CHARGING STUDY

by Carolyn K. Purvis

Lewis Research Center

SUMMARY

A model to predict charging effects in the Jovian magnetosphere was developed for the preliminary design of a Jupiter probe. Charging calculations using this model are presented and discussed. At distances from Jupiter of less than 14.6 Jovian radii, differential charging of interior structures relative to adjacent exterior surfaces may be as much as 15.4 kilovolts. Kilovolt differentials are also predicted between the sunlit and dark exterior surfaces of the probe and in the region of the Jovian magnetosphere where corotation of the low-energy plasma affects ion collection. Design modifications to reduce these differentials are recommended.

INTRODUCTION

Electrostatic charging of spacecraft surfaces to kilovolt potentials occurs when clouds of energetic particles are injected into the midnight region of the magnetosphere near synchronous altitude during geomagnetic substorm activity. The first evidence of spacecraft charging to kilovolt potentials was reported by DeForest (ref. 1) in 1972, based on data from the University of California at San Diego (UCSD) plasma detector on the ATS-5 spacecraft. Since that time, a number of workers have studied aspects of the spacecraft charging phenomena. Grard (ref. 2) and Rosen (ref. 3) provide extensive information on the subject. Existing knowledge of spacecraft charging was used in this study to develop a theory that would predict charging for a Jupiter probe in the Jovian magnetosphere.

Any surface immersed in a charged-particle environment will come into equilibrium with it by acquiring a potential such that in steady state the net current to the surface is zero. Since for most plasmas the electron flux is much larger than the ion flux, the surface acquires a negative potential. Most materials respond to charged-particle bombardment by backscattering or reflecting electrons and by emitting secondary electrons. These emitted particles effectively reduce the electron current to the surface and thus

reduce the negative potential. In addition, illuminated surfaces emit photoelectrons, which contribute an additional outgoing electron current.

Thus it is not surprising that spacecraft can become charged by their environments. What was surprising in the geosynchronous case was that the particles injected into the magnetosphere by geomagnetic substorms have kilovolt energies and thus can charge spacecraft surfaces to kilovolt potentials.

The Jovian magnetosphere has large fluxes of energetic particles. Scarf and Fredericks (ref. 4) suggest that these particles may interact with spacecraft, possibly charging their surfaces to large potentials. In addition, because many of these particles have sufficient energy to penetrate into the interior of a spacecraft, a spacecraft's interior structures may become charged relative to its exterior surfaces if they are electrically isolated from each other. This "inside out" charging is possible for the Jupiter probe since the proposed exterior surface is entirely insulating and its metal structure has no electrical access to the exterior.

Because of concern about possible charging effects on the Jupiter probe's performance, an analytical study was performed. The specific objectives of the study were to investigate the possible charging of both the exterior and interior surfaces of the probe during its descent through the Jovian magnetosphere and to make design recommendations to minimize identified charging problems. This report describes this charging study and presents and discusses the results.

Jon C. Oglebay of the Lewis Research Center wrote, debugged, and ran the computer program used in this study.

JOVIAN CHARGED-PARTICLE ENVIRONMENT

A model of the charged-particle environment in the Jovian magnetosphere, based on data from the Pioneer 10 and 11 spacecraft (ref. 5), has been developed by the Jet Propulsion Laboratory. This model gives fluxes of high-energy particles in the Jovian magnetosphere and the characteristic temperatures of the magnetospheric plasma components: ~4 eV for electrons, ~100 eV for protons inside about 6 Jovian radii, and ~400 eV for protons from 6 radii to the magnetopause (~60 radii). These low-energy plasma components are assumed to be Maxwellian and are hereinafter called thermal. Because they are trapped by the planet's magnetic field, they corotate with Jupiter.

The fluxes of high-energy particles are considered to be isotropic in this model. They are not expected to be Maxwellian and do not corotate with Jupiter. In this study, "high energy" particles are electrons with energies from 0.06 to 100 MeV and ions with energies from 1 to 100 MeV. The limits on these energy ranges are the lowest and highest energies for which information was available. Figure 1 shows the fluxes of thermal electrons ($\epsilon_e > 0$) and protons ($\epsilon_p > 0$) and of high-energy electrons ($\epsilon_e > 0.06$ MeV) and

protons ($\epsilon_p > 1$ MeV) in this study as a function of time to Jovian encounter along a possible mission trajectory. The long ticks on the abscissa indicate times for which probe potentials were calculated.

In the present study of Jupiter probe charging, the high-energy and thermal (low energy) currents are modeled separately. Their values are then combined to achieve the required current balance because the dependence of the particle currents on the probe surface voltages is expected to be different for the low- and high-energy particles.

JUPITER PROBE MODEL

The Jupiter probe configuration studied here has a blunted, 60° half-angle, conical forebody and a hemispherical afterbody. The forebody is a carbon-phenolic, ablative heat shield that protects the aluminum interior structure and instrumentation. The afterbody is a fiberglass-phenolic, honeycomb hemisphere (45-cm spherical radius) that protects the antenna. The outer surfaces of both the forebody and the afterbody are covered with multilayer-aluminized-Mylar thermal blankets. For the charging model, the probe is considered a sphere of 45-centimeter radius. Figure 2 shows the probe configuration and the spherical model.

The probe is separated from the orbiter 57 days before Jupiter encounter (at about 500 Jovian radii) and coasts toward the planet on a near-zero-inclination trajectory at a nominal spin rate of 5 rpm about its axis of symmetry. During the coast, the afterbody is oriented toward the Earth. As the probe enters the sensible atmosphere (altitude of ~450 km), it tips about 90° so that the forebody heat shield points toward Jupiter and the afterbody toward the orbiter. Nominal velocity before entry is about 60 km/sec. The probe and the mission are described in detail in references 6 and 7.

Since the coast phase of the mission is of primary interest for the charging study, the relative geometry assumed in the model approximates that of the coast phase. This geometry is shown in figure 3. Because the Sun is assumed to be in the same direction as the Earth relative to the probe, the afterbody is sunlit and the forebody, dark. In addition, the probe's velocity vector is assumed to be perpendicular to the radial line connecting the center of Jupiter to the center of the probe. In this way the effects of the relative motion of the probe and the thermal plasma - which, as noted in the previous section, corotates with the planet - on particle current collection can be more easily calculated.

As a quick review of the probe's structure, the exterior surface is completely covered by insulating thermal blankets, the entire afterbody is an insulating structure, and the conducting aluminum structure is in the forebody. If the aluminized layers of the thermal blankets are not grounded to the aluminum structure, the only mechanisms for charge transfer from the forebody to the afterbody are leakage along the insulator

surfaces or leakage through the sheath. The present model treats the forebody and afterbody as independent, an assumption that affects the predicted voltage differences between the forebody and afterbody surfaces as discussed in the results section.

The model currents are defined in figure 4. The equilibrium potentials for the four surfaces of interest are φ_f for the exterior surface of the forebody, φ_{Al} for the aluminum structure that forms the interior surface of the forebody, φ_a for the exterior surface of the afterbody, and φ_{ar} for the interior surface of the afterbody. The currents $I_{HE,f}$ and $I_{HE,a}$ are caused by high-energy particles impinging on the forebody and afterbody exterior surfaces, respectively. These particles include electrons and protons that are incident on the surfaces but do not have sufficient energy to completely penetrate the appropriate insulating layers, as well as the backscattered and secondary electrons generated by them. The net currents $I_{TH,f}$ and $I_{TH,a}$ are caused by thermal plasma particles impinging on the forebody and afterbody exterior surfaces, respectively. These particles include both primary and secondary (emitted) particles. The photocurrents $I_{PHO,f}$ and $I_{PHO,a}$ are emitted by the respective surfaces. The leakage currents through the bulk of the insulators are $I_{L,f}$ and $I_{L,a}$. The current $I_{HEP,a}$ is caused by high-energy protons and electrons that have penetrated to the aluminum structure through either the forebody or afterbody insulators and are stopped by the aluminum structure. In addition, those particles coming through the afterbody insulators that have insufficient energy to penetrate completely through the probe and escape contribute to this current. Thus, $I_{HEP,a}$ is the particle current directly incident on the aluminum structure. The current $I_{HEP,f}$ is caused by high-energy particles that have penetrated both the forebody insulators and the aluminum structure but cannot penetrate completely through the probe and escape. Thus, $I_{HEP,f}$ is the particle current directly incident on the interior surface of the afterbody.

In summary, the charging environment for the exterior surfaces consists of currents caused by high-energy particles, thermal plasma particles, and photons. The charging environment for the interior surfaces consists of currents caused by high-energy particles. The interior and exterior surfaces are connected by leakage paths through the insulating layers.

PROBE CURRENT BALANCES

Thermal Plasma and Photoelectron Currents

The thermal plasma currents to the probe include contributions from primary electrons and ions and from secondary electrons due to electron impact. That is, they are of the form

$$I_{TH}(\varphi_s) = -I_e(\varphi_s) + I_i(\varphi_s) + I_s(\varphi_s) \tag{1}$$

where φ_s is the appropriate surface voltage and I_e, I_i, and I_s are the primary electron, primary ion, and secondary electron currents, respectively. The ion currents also depend on whether the probe is at rest or in motion with respect to the corotating plasma: At distances nearer the planet than about 23 Jovian radii, the probe is effectively at rest; further from the planet, the probe is in motion. That is, at 23 Jovian radii or less, the ion thermal velocity is greater than the relative velocity of the probe and the corotating plasma; at 23 Jovian radii or more, the relative velocity exceeds the ion thermal velocity.

Table I summarizes the functional forms for the thermal and photoelectron currents to the probe, for the geometry of figure 3. Figure 5 shows the thermal and photoelectron currents to the probe. These currents and their functional forms are discussed in more detail in appendix A.

High-Energy-Particle Currents

Fluxes of high-energy particles can charge both the exterior and interior surfaces of the probe since some particles will penetrate into the interior. The currents caused by high-energy particles impinging on the probe should not be affected by the probe's surface voltages unless these voltages become comparable to the particle energies. These currents are therefore considered to be independent of φ_s until $|e\varphi_s|$ becomes approximately 0.06 MeV.

The information on high-energy particle fluxes used in the present study is in terms of integral fluxes of electrons and ions along the probe's trajectory. Currents caused by particles with energies greater than ϵ_1 can be found from expressions of the form

$$I = \frac{1}{2} Ae\Gamma(\epsilon_1) \tag{2a}$$

where A is the surface area of interest, e is the electronic charge, and $\Gamma(\epsilon_1)$ is the integral flux at ϵ_1 (i.e., the flux of particles with energies equal to or less than ϵ_1). Currents caused by particles with energies between ϵ_1 and ϵ_2 ($\epsilon_2 > \epsilon_1$) can be found from expressions of the form

$$I = \frac{1}{2} Ae\left[\Gamma(\epsilon_1) - \Gamma(\epsilon_2)\right] \tag{2b}$$

The factor of 1/2 in each of these equations accounts for the fact that the model used to calculate the fluxes assumes an isotropic particle distribution: Only half the particles will have velocities directed toward the probe.

Figure 6 depicts the behavior of high-energy particles impinging on the probe. Particles impinging from the forward direction but unable to completely penetrate the forebody insulating layers ($\epsilon < \epsilon_f$) and those impinging from the aft direction but unable to completely penetrate the afterbody insulating layers ($\epsilon < \epsilon_a$) are considered to contribute to the currents to the forebody and afterbody exterior surfaces, respectively.

Particles impinging from the forward direction with energy ϵ_f or greater but unable to completely penetrate the aluminum structure and enter the afterbody region ($\epsilon_f \leq \epsilon < \epsilon_{f,Al}$) and particles impinging from the aft direction with energy ϵ_a or greater but unable to completely penetrate the probe and escape ($\epsilon_a \leq \epsilon < \epsilon_e$) are considered to constitute the currents to the internal aluminum structure. All particles approaching from the aft direction that would be stopped either in the aluminum structure itself or in the forebody insulators are considered to constitute a current to the aluminum structure, which is effectively the interior surface of the forebody. Those particles approaching from the forward direction with energies $\epsilon_{f,Al}$ or greater but unable to also penetrate the afterbody insulators and escape ($\epsilon_{f,Al} \leq \epsilon < \epsilon_e$) are considered to contribute to the current to the inside of the afterbody. Finally, particles from either direction with sufficient energy to penetrate completely through the probe and thus escape ($\epsilon \geq \epsilon_e$) are not considered sources of charging current to any part of the probe.

These assumptions about the high-energy particle currents ignore the effects of charge deposition in the insulator bulk. Although consideration of such effects is beyond the scope of this study, it is warranted in further work. Each of these energies (ϵ_f, $\epsilon_{f,Al}$, etc.) is different for electrons and ions since ions have much smaller penetrating ranges in materials than electrons of the same energy. This is accounted for in the model. Expressions used for the various high-energy currents are summarized in table II. Their functional forms are discussed in more detail in appendix B.

Current Balances

The current balance is solved to determine the potentials as follows: Balancing the forebody current requires that the net currents to both the heat-shield exterior and the aluminum structure be zero. Thus,

$$0 = I_{HE,f}(\varphi_f) + I_{TH,f}(\varphi_f) - I_{PHO,f}(\varphi_f) - I_{L,f}(\varphi_f, \varphi_{Al}) \tag{3}$$

and

$$0 = I_{HEP,a}(\varphi_f) + I_{L,f}(\varphi_f, \varphi_{Al}) \tag{4}$$

The leakage current through the shield depends on the difference between φ_f and φ_{Al} so that

$$I_{L,f} = \frac{\varphi_f - \varphi_{Al}}{R_f} \tag{5}$$

where R_f is the resistance of the forebody insulators. Eliminating $I_{L,f}$ from equations (3) and (4) yields

$$0 = I_{HE,f}(\varphi_f) + I_{TH,f}(\varphi_f) - I_{PHO,f}(\varphi_f) + I_{HEP,a}(\varphi_f) \tag{6}$$

which can be solved for φ_f.[1] Then φ_{Al} is calculated from equations (4) and (5).

Similarly, balancing the afterbody current requires that the net currents to both the interior and exterior surfaces of the afterbody be zero. The equations, analogous to equations (3) to (5), are

$$0 = I_{HE,a}(\varphi_a) + I_{TH,a}(\varphi_a) - I_{PHO,a}(\varphi_a) - I_{L,a}(\varphi_a, \varphi_{ar}) \tag{7}$$

$$0 = I_{HEP,f}(\varphi_a) + I_{L,a}(\varphi_a, \varphi_{ar}) \tag{8}$$

$$I_{L,a} = \frac{\varphi_a - \varphi_{ar}}{R_a} \tag{9}$$

where R_a is the resistance of the afterbody insulators. After φ_a is found from equations (7) and (8),[1] φ_{ar} can be determined from equations (8) and (9).

Specific Probe Parameters

Solving the current-balance equations requires assigning numerical values to a number of parameters that depend on the materials and construction of the probe: surface areas, resistances, secondary emission and backscattering coefficients, penetration energies for the high-energy particles, etc. Table III shows each parameter, its symbol, the value used in this model, and the basis on which this value was chosen. Values for

[1]The currents are expressed as functions of the potentials in tables I and II.

the backscattering and secondary emission coefficients were, as indicated, estimated from ranges or estimates given in references. Values for the resistance and the penetration energies were calculated from several pieces of information (appendix C).

RESULTS AND DISCUSSION

The current-balance equations were used to calculate the equilibrium potentials of the forebody exterior surface φ_f, the aluminum structure φ_{Al}, the afterbody exterior surface φ_a, and the afterbody interior surface φ_{ar} for the positions along the probe's trajectory indicated in figure 1. The transition from "in motion" to "at rest" (at 23 Jovian radii) takes place about 24.5 hours before Jovian encounter. (See appendix A for further discussion of this transition.)

Forebody Potentials

Potentials predicted for the forebody exterior surface φ_f and the aluminum interior structure φ_{Al} are shown as functions of position and time to Jovian encounter in figure 7. Significant charging of the forebody exterior surface with respect to the plasma occurs from 7 to 14 hours and more than 24 hours before encounter. These times correspond to distances from the planet of 9 to 15 Jovian radii and more than 23 Jovian radii, respectively. Because in the latter region the probe is in motion with respect to the corotating plasma, the ion component of the thermal plasma current is cut off in this model. Because the forebody exterior surface is in the dark, the only source of ion current to it is the high-energy ions. The flux of these ions is very low (fig. 1). There is charging from 7 to 14 hours before encounter probably because the thermal plasma is simply insufficient to balance the effects of the high-energy electrons. The most negative potential φ_f predicted here is -18 kilovolts at 12 hours, or 13 Jovian radii. These predicted potentials are overly pessimistic in regions where large differentials are expected between the forebody and afterbody exterior surfaces, as discussed on page 10.

The aluminum structure is also predicted to charge in two regions: More than 24 hours before Jovian encounter, φ_{Al} is about equal to φ_f. Less than 14 hours before encounter, φ_{Al} is more negative than φ_f; φ_{Al} reaches its most negative potential (-21 kV) at 11 and 12 hours. In addition to this "absolute" charging (with respect to the plasma), there is significant differential charging between the aluminum structure and the forebody exterior surface less than 14 hours before encounter. This aspect is discussed in the section Differential Charging.

Afterbody Potentials

Potentials predicted for the interior φ_{ar} and exterior φ_a afterbody surfaces are shown as functions of position and time to Jovian encounter in figure 8. The afterbody exterior surface experiences almost no charging and is generally a few volts positive. No significant changes occur in the transition from motion to rest. The photocurrent apparently maintains the potential very near plasma ground. The afterbody interior shows some charging less than 9 hours before Jovian encounter, or less than 11 Jovian radii, but the charging is much less severe than for the forebody exterior surface. Its maximum negative potential is -195 volts, which is not very significant from a charging standpoint.

Differential Charging

Figures 7 and 8 indicate two possible problems in differential charging: the differential between the forebody exterior surface and the aluminum interior structure and that between the forebody and afterbody exterior surfaces. There is also a differential between the aluminum interior structure and the afterbody interior surface, but solving the first two problems should automatically solve it as well.

Figure 9 shows the differential potentials $\varphi_{Al} - \varphi_f$ and $\varphi_f - \varphi_a$ as functions of time to encounter. It is notable that φ_{Al} is always more negative than or equal to φ_f and that φ_f is more negative than φ_a.

Differential across forebody insulators. - There is a kilovolt potential across the forebody insulators (fig. 9) less than 13 hours (14.6 Jovian radii) before encounter, with a maximum of 15.4 kilovolts at 9 hours (11 radii). The probe forebody is composed of the Mylar thermal blankets, the carbon-phenolic heat shield, and a fiberglass structure (fig. 13). In obtaining the overall resistance of the forebody insulator, these components were treated as resistors in series (appendix C). If these resistors behave as a voltage divider, the 15.4 kilovolts across the insulators yields 8.7 kilovolts across the Mylar, 6.7 kilovolts across the fiberglass, and $\sim 5 \times 10^{-6}$ volts across the heat shield. These voltages indicate stresses of $\sim 3 \times 10^{7}$ volts per meter (~750 V/mil) on the Mylar and $\sim 3 \times 10^{5}$ volts per meter (~7.5 V/mil) on the fiberglass. Since the dielectric strength of Mylar is several thousand volts per mil, this stress should not cause bulk breakdowns of the Mylar. However, it may present a problem at edges or corners, where field intensification is expected, and which are thus the most probable regions for arc breakdowns to occur. The present model cannot treat edges and corners. Assessing the fields in such regions requires a more detailed model of the surfaces.

These voltage stresses probably would present a serious problem. However, since there is differential charging, care should be taken to consider its possible effects. For

example, simply tying the aluminized layers of the Mylar to spacecraft ground, in the standard fashion, may cause all the differential potential to appear across the external Mylar film and thus approach and perhaps exceed Mylar's dielectric strength. Two simple ways to minimize the differential potentials in the forebody insulators might be to metalize and ground the exterior of the Mylar or remove the Mylar entirely, and then in each case to install a grounded conductive layer between the fiberglass and the heat shield or otherwise provide a conductive path around the fiberglass to the aluminum structure. ("Ground" here refers to attachment to the aluminum structure.)

Differential between forebody and afterbody exteriors. - The potential difference between the forebody and afterbody exterior surfaces is shown as the dashed line in figure 9. Differentials to 18 kilovolts are predicted from 7 to 14 hours before encounter and differentials to 300 kilovolts, more than 24 hours before encounter. These predictions are based on spherical probe theory and the assumption of ion shadowing more than 24 hours before encounter. The negative hemisphere of a strongly differentially charged sphere can collect more ion current than one hemisphere of a sphere uniformly charged to the same large negative potential. Thus the potentials predicted for the forebody are more negative than if a more accurate asymmetrical model were used. Estimates of the effects of asymmetry indicate that kilovolt differentials can still be expected. From 7 to 14 hours before encounter, the maximum differential is estimated to be at least 9 kilovolts; more than 24 hours before encounter, a few kilovolts (rather than 300 kV) is estimated. Clearly, in reality the differential potential will not appear as a step change at the forebody-afterbody boundary, since effects such as surface leakage and charge transport in the photoelectron sheath will assure a smooth transition. If the differential is distributed uniformly along the surfaces from forward to aft, the semicircumference πr_p of 1.41 meters indicates fields of $\sim 1.3 \times 10^4$ volts per meter along the surface for the 18-kilovolt total differential and $\sim 10^5$ volts per meter for the 3×10^5-volt differential. If the differential is distributed other than linearly, there will be areas in which the stresses will be even larger. How the photoelectron sheath will behave in transferring charge from forward to aft is beyond the scope of this study, but it bears further investigation as the photocurrent is the critical factor in maintaining the afterbody surface potential near zero.

Making the forebody surface relatively conducting would reduce the forebody-afterbody differential by allowing charge from the forebody surface to migrate freely. The forebody shield should also be electrically connected to sunlit areas so that photoelectron emission can remove electrons and reduce the negative charge. A photoelectron sheath could extend far enough to perform this function to some degree. But the best solution is to make the afterbody exterior surface conductive and connect it electrically to the forebody surface. If this is not possible, a conducting annular structure electrically connected to the forebody surface and exposed to sunlight should be

considered. However, any such structure will collect additional charged particles as well as additional photons.

CONCLUSIONS AND RECOMMENDATIONS

The Jupiter probe, as presently conceived, may have problems related to differential charging since kilovolt potential differences develop between interior and exterior structures and between sunlit and dark surfaces. Although the voltage stresses across the bulk of the forebody insulators are predicted to be well below the bulk breakdown voltages of the insulators, edges and corners may present a problem. These voltage gradients can be minimized by incorporating relatively simple design changes. The differential between light and dark surfaces has less clear effects since their severity depends on the actual voltage distributions and material strengths. Again, it seems best to minimize such effects, and a simple design modification appears feasible.

The following modifications are recommended to minimize differential charging:

1. The forebody exterior surface should be made more electrically conductive by either removing the Mylar or metalizing the exterior surface. If the Mylar is metalized, all metalized layers of the thermal blankets, including the surface layer, should be grounded to the aluminum structure.

2. An electrically conductive path should be created around the fiberglass, connecting the inside of the carbon-phenolic heat shield to the aluminum structure. The afterbody surface should be made electrically conductive; or a conducting structure, perhaps a metal band or ring, should be added to give the shaded (now conductive) forebody surface electrical access to photoelectrons in order to reduce the light-dark differential voltages.

With these modifications, particularly with the electrically conductive afterbody surface, differential charging should be reduced to a minimum. This is true even if the environment is different from the one used in the model. The modifications do not, however, guarantee that the probe as a whole will remain near plasma ground. If the probe must be maintained near plasma ground (e.g., for preentry scientific experiments), some type of potential-control device such as an electron emitter may be needed.

This study also indicates some areas in which additional analysis would be useful: voltage asymmetry effects on particle collection; charge transport between the sunlit and dark surfaces, both through the sheath and along surfaces; electric fields in the afterbody cavity; and charge trapping in the insulator bulk.

Lewis Research Center,
National Aeronautics and Space Administration,
Cleveland, Ohio, March 30, 1978,
506-23.

APPENDIX A

CURRENTS DUE TO THERMAL PLASMA FLUXES AND PHOTOELECTRONS

For purposes of calculating the thermal currents to a Jupiter probe, the probe is assumed to be smaller than a Debye length so that orbit-limited theory applies. The thermal plasmas are assumed to be Maxwellian and to corotate with the Jovian magnetosphere, an assumption that affects the ion collection in regions where the probe velocity relative to the plasma is greater than the ion random thermal velocity. Electron collection is not affected.

Primary Particle Currents

Electrons. - For a spherical collection geometry, currents due to collection of incident primary electrons are given by

$$I_e = j_{eo} A \exp\left(\frac{e\varphi_s}{kT_e}\right) \quad \text{for} \quad \varphi_s \leq 0 \tag{A1a}$$

$$I_e = j_{eo} A \left(1 + \frac{e\varphi_s}{kT_e}\right) \quad \text{for} \quad \varphi_s > 0 \tag{A1b}$$

where A is the surface area; φ_s, the surface potential; e, the electronic charge; and kT_e, the electron temperature. Here, j_{eo} is the random thermal current density, which is given by

$$j_{eo} = N_e e \left(\frac{kT_e}{2\pi M_e}\right)^{1/2} = \frac{e\Gamma_{eo}}{4} \tag{A2}$$

where N_e is the electron number density; M_e, the electron mass; and Γ_{eo}, the integral flux of electrons.

Ions. - Since the thermal plasma is corotating with Jupiter, its corotation velocity is given by

$$v = W_J R = 12.5\, R_J \text{ km/sec} \tag{A3}$$

where W_J is the angular frequency of Jupiter's rotation; R, the distance from Jupiter's axis of rotation; and R_J, the distance from the axis of Jupiter in Jovian radii. This velocity and the random thermal velocities of ions are plotted in figure 10 as functions of distance from Jupiter. The corotation velocity v exceeds the thermal velocity of ions at distances from the planet greater than about 23 Jovian radii.

In regions where the probe is essentially at rest with respect to the plasma (i. e., at less than 23 Jovian radii), the ion currents are found from

$$I_{i2} = j_{io} A \exp\left(-\frac{e\varphi_s}{kT_i}\right) \quad \text{for} \quad \varphi_s \geq 0 \tag{A4a}$$

$$I_{i2} = j_{io} A \left(1 - \frac{e\varphi_s}{kT_i}\right) \quad \text{for} \quad \varphi_s \leq 0 \tag{A4b}$$

where kT_i is the ion temperature and j_{io}, the ion random current density defined by

$$j_{io} = N_i e \left(\frac{kT_i}{2\pi M_i}\right)^{1/2} = \frac{e\Gamma_{io}}{4} \tag{A5}$$

where N_i is the ion number density; M_i, the ion mass; and Γ_{io}, the integral flux of ions.

In regions where the probe is in motion with respect to the plasma (i. e., at 23 Jovian radii or more), ion currents to the forebody and afterbody surfaces will be different. This situation is illustrated in figure 11. Whipple (ref. 8) gives the ion current to the forebody surface as

$$I_{i1} = 2r_p^2 N_i e V \left(1 - \frac{2e\varphi_s}{M_i V^2}\right) \quad \text{for} \quad \varphi_s > 0 \tag{A6a}$$

$$/ \quad \frac{2e\varphi_s}{2}\Bigg) < \lambda_D \tag{A6b}$$

When φ_s is sufficiently negative that condition (A6b) is not satisfied,

$$I_{i1} = N_i e \alpha_i \pi r_p^2 \left[\frac{\Gamma \pi \alpha_i}{V} \operatorname{erf}\left(\frac{V}{\alpha_i}\right)\left(\frac{e\varphi_s}{kT_i} + \frac{V^2}{\alpha_i^2} + \frac{1}{2}\right) \exp\left(-\frac{V^2}{\alpha_i^2}\right)\right] \tag{A6c}$$

In these equations, r_p is the probe radius; λ_D, the Debye length; α_i, the ion thermal velocity; and V, the relative velocity of the plasma and probe. For the geometry depicted in figure 3, these forebody surface ion currents will impinge on the afterbody of the probe, and V will be given by

$$V = v - 59 \text{ km/sec} \tag{A7}$$

where v is defined in equation (A3) and 59 km/sec is the probe's velocity. For an electron plasma component having $kT_e = 4$ eV and $N_e = 1$ per cm^3 and for H^+ ions, condition (A6b) will be satisfied unless φ_s becomes more negative than about 4×10^5 volts. Since the afterbody is also sunlit (fig. 3), such a high negative potential is very unlikely. Therefore, equation (A6a) has been used in the present model.

When the probe is in motion with respect to the plasma, there will be a relatively large void of ions "behind" the probe so that the side that is not being bombarded by the corotating ions (in this case the forebody shield) will effectively see no ion current.

Emitted Currents

Particle currents may be emitted by photoemission, reflection and backscattering of primary electrons, reflection of primary ions, and emission of secondary electrons due to ion and electron impact. From Whipple's analysis (ref. 8), for 4-eV electrons and 100- to 400-eV ions the effects of reflection (for both electrons and ions) and of secondary-electron emission due to ion impact should be small (less than about 5 percent of primary currents). No backscattering of electrons is expected for primaries with energies less than 100 eV. Thus the emitted currents of importance here are photocurrent and current due to secondary electrons released by electron impact.

Photoelectrons. - From the estimated density (1.8×10^{-10} A/cm^2) of a typical photocurrent from a surface at Jupiter, the sunlit half of the probe (the afterbody) will emit a photocurrent of

$$I_{PHO} = 1.8 \times 10^{-10} A_a \quad \text{for} \quad \varphi_a \leq 0 \tag{A8a}$$

$$I_{PHO} = 1.8\times10^{-10} A_a \exp\left(-\frac{e\varphi_a}{kT_{ph}}\right) \quad \text{for} \quad \varphi_a > 0 \tag{A8b}$$

where A_a and φ_a are, respectively, the area and potential of the afterbody surface; and kT_{ph} is the temperature of the emitted photoelectrons. In the present analysis kT_{ph} is assumed to be 2 eV. The exponential term in equation (A8b) accounts for the reattraction of emitted photoelectrons to a positive surface.

Secondary electrons released by electron impact. - The yield of secondary electrons released by electron impact is a function of the energy of the primary electrons and of the material properties. A functional form for this yield, attributed to Sternglass, has been given by Grard, et al. (ref. 9). The material properties needed are the maximum yield δ_m and the primary impact energy ϵ_m at which the maximum yield is attained. Willis and Skinner (ref. 10) give $\delta_m = 4.8$ and $\epsilon_m = 175$ eV for Mylar, which constitutes the outer surface of the probe. The yield curve and the functional form for the yield are given in figure 12. Using this expression for secondary yield, Purvis, et al. (ref. 11) find

$$I_s = A\pi j_{eo} 7.4\, \delta_m \frac{kT_e}{\epsilon_m} 5!\, i^5 \operatorname{erfc}\left(\sqrt{\frac{kT_e}{\epsilon_m}}\right) \exp\left(\frac{kT_e}{\epsilon_m} + \frac{e\varphi_s}{kT_e}\right) \quad \text{for} \quad \varphi_s \le 0 \tag{A9a}$$

where $i^5 \operatorname{erfc}\sqrt{kT_e/\epsilon_m}$ is the fifth repeated integral of the error function complement. Equation (A9a) depends on φ_s in a simple manner. It is more convenient to express this current density by

$$I_s = Aj_{so} \exp\left(\frac{e\varphi_s}{kT_e}\right) \quad \text{for} \quad \varphi_s \le 0 \tag{A9b}$$

where

$$j_{so} \equiv \pi j_{eo} 7.4\, \delta_m \frac{kT_e}{\epsilon_m} 5!\, i^5 \operatorname{erfc}\left(\sqrt{\frac{kT_e}{\epsilon_m}}\right) \exp\left(\frac{kT_e}{\epsilon_m}\right)$$

is a constant for each combination of electron environment and material properties.

The appropriate expression for $\varphi_s > 0$ is quite complex. However, for $\varphi_s > 0$, the emitted secondaries will be attracted back to the surface so that their total contribution to the current balance will become small as φ_s becomes positive. For simplicity, the expression chosen for I_s in this case is

$$I_s = Aj_{so} \exp\left(-\frac{e\varphi_s}{kT_s}\right) \quad \text{for} \quad \varphi_s > 0 \tag{A9c}$$

where kT_s is the temperature of the secondaries. This temperature is expected to be a few electron volts. The present analysis uses $kT_s = 2$ eV.

Magnetic Field Effects

Two effects of Jupiter's magnetic field on current collection were considered: gyration around the magnetic field and induced $\vec{V} \times \vec{B}$ potential gradients. Neither is thought to be of great significance for probe charging, since they probably will affect potential by only a few tens of volts. Whipple (ref. 8) discusses the nature of the effects in more detail.

Gyration around magnetic field. - Charged particles in a magnetic field will gyrate about the field lines with a radius of gyration given by

$$\rho^* = \sqrt{\frac{2MkT}{eB}} \tag{A10}$$

where B is the magnetic induction. If ρ^* becomes smaller than the radius of the probe, the electron current to the probe will be reduced. Since ions have much larger radii of gyration than electrons, their collection is unaffected. Present calculations indicate that at about 3 Jovian radii the thermal electron current will be reduced to 90 percent of its value with no magnetic field; and at about 1.4 Jovian radii, to about 55 percent. Estimates of the effect of this decrease on probe potential indicate that φ_s will become less than 10 volts more positive at 1.4 Jovian radii, an insignificant amount for charging considerations.

Induced $\vec{V} \times \vec{B}$ potential gradients. - The motion of the probe across the magnetic field of Jupiter gives rise to a potential gradient across the probe in the $\vec{V} \times \vec{B}$ direction, where $\vec{V}$ is the velocity of the probe relative to the magnetic field $\vec{B}$. Since $\vec{B}$ corotates with Jupiter, this $\vec{V}$ is the same as the velocity of the probe relative to the the corotating plasma (eq. (A7)). For the geometry of figure 3, if the magnetic dipole were alined with the Jovian axis of rotation, the gradient would be in the radial direction and would result in an estimated 10-percent reduction in the electron current at about 1.5 Jovian radii. The potential gradient across the probe at 1 Jovian radius is estimated as about 20 volts. Because this is a small effect from the charging standpoint, the probe's spin would reduce the gradient below the calculated values. The effect could become significant for a larger spacecraft, since the 20 volts calculated here represents the development of a gradient of about 20 volts per meter.

The thermal and photoelectron currents to the forebody and afterbody exterior surfaces are calculated from

$$I_{TH} + I_{PHO} = -I_e + I_i + I_s + I_{PHO} \tag{A11}$$

Expressions for the four righthand terms are given in table I for the conditions used in this analysis. The term I_i is actually I_{i1} or I_{i2} depending on whether the probe is effectively in motion (region 1, use I_{i1}) or at rest (region 2, use I_{i2}) with respect to the plasma. Entries subscripted a refer to afterbody parameters; those subscripted f refer to forebody parameters. Some currents in equation (A11) are zero for certain cases. For example, $I_{PHO} = 0$ on the shadowed half of the probe (the forebody) and $I_i = 0$ on the afterbody side in region 1. Figure 5 depicts the nonzero plasma and photoelectron currents to the probe in regions 1 and 2.

APPENDIX B

CURRENTS DUE TO HIGH-ENERGY PARTICLES

Since some high-energy particles can penetrate into the interior of the probe, charging of both the exterior and interior surfaces can be expected. The situation is depicted in figure 6 and discussed in the main body of this report.

Currents to Exterior Surfaces

High-energy particle currents to the exterior surfaces are due to particles with energies $\epsilon < \epsilon_f$ for the forebody surface and $\epsilon < \epsilon_a$ for the afterbody surface. Electron current to the forebody surface is given by

$$I_{He} = \frac{1}{2} A_f e \left[\Gamma_e(\epsilon_{01}) - \Gamma_e(\epsilon_{f1})\right] \tag{B1}$$

where the Γ_e is electron flux, ϵ_{01} is the lowest high energy being considered for electrons, and ϵ_{f1} is the electron energy required to completely penetrate the forebody insulating layers (ϵ_f for electrons). The current due to incident high-energy ions (H^+) is similarly defined by

$$I_{Hi} = \frac{1}{2} A_f e \left[\Gamma_i(\epsilon_{02}) - \Gamma_i(\epsilon_{f2})\right] \tag{B2}$$

where the Γ_i is ion flux, ϵ_{02} is the lowest high energy for ions, and ϵ_{f2} is the ion energy required to completely penetrate the forebody insulating layers (ϵ_f for ions). Currents to the afterbody exterior surface that are due to incident high-energy electrons and ions are defined in a similar fashion, with A_f replaced by A_a and ϵ_{f1} and ϵ_{f2} replaced by ϵ_{a1} and ϵ_{a2}, where ϵ_{a1} and ϵ_{a2} are, respectively, the afterbody energies for electrons and ions.

Emission processes such as electron reflection and secondary-electron emission by electron impact are insignificant for these high-energy particles. However, electron backscattering and secondary-electron emission by proton impact can be significant. Because backscattered electrons are taken to be a fixed fraction of incident electrons,

$$I_{BS} = \zeta I_{He} \tag{B3}$$

where ζ is the backscatter coefficient. Backscattered electrons are assumed to escape.

Secondary-electron emission by ion impact I_{SP} is similarly taken to represent a fixed fraction of the incident ion current. However, these secondaries leave the surface with low energies, comparable to the energies of secondary electrons released by electron impact (i. e., a few volts). Thus,

$$I_{SP} = \delta_p I_{Hi} \quad \text{for} \quad \varphi_s \leq 0 \tag{B4a}$$

$$I_{SP} = \delta_p I_{Hi} \exp\left(-\frac{e\varphi_s}{kT_S}\right) \quad \text{for} \quad \varphi_s > 0 \tag{B4b}$$

where δ_p is the coefficient for secondary-electron emission by ion impact.

Currents to Internal Surfaces

Particle currents to the aluminum structure are, as discussed, caused by particles impinging from the forward direction with energies $\epsilon_f \leq \epsilon < \epsilon_{f,Al}$ and to those impinging from the aft direction with energies $\epsilon_a \leq \epsilon < \epsilon_e$. If we maintain the convention of an added subscript 1 for electron energy, and an added subscript 2 for ion energy, these current contributions can be expressed as follows:

For electrons from the forward direction,

$$I_{He,f} = \frac{1}{2} a_f e \left[\Gamma_e(\epsilon_{f1}) - \Gamma_e(\epsilon_{f,Al,1})\right] \tag{B5}$$

For electrons from the aft direction,

$$I_{He,Al} = \frac{1}{4} A_f e \left[\Gamma_e(\epsilon_{a1}) - \Gamma_e(\epsilon_{e1})\right] \tag{B6}$$

where there is an additional factor of 1/2 in equation (B6) because these electrons are considered to be collected by the flat part of the aluminum structure $\left(\text{area of } \pi r_p^2\right)$ instead of the hemispherical part $\left(\text{area of } 2\pi r_p^2\right)$.

For ions from the forward direction,

$$I_{Hi,f} = \frac{1}{2} A_f e \left[\Gamma_i(\epsilon_{f2}) - \Gamma_i(\epsilon_{f,Al,2})\right] \tag{B7}$$

For ions from the aft direction,

$$I_{Hi,Al} = \frac{1}{4} A_f e \left[\Gamma_i(\epsilon_{a2}) - \Gamma_i(\epsilon_{e2})\right] \tag{B8}$$

Particle current to the interior of the afterbody insulating layers is caused by particles approaching from the forward direction with energies $\epsilon_{f,Al} \leq \epsilon < \epsilon_e$. Thus, for electrons

$$I_{He,a} = -\frac{1}{2} A_a e \left[\Gamma_e(\epsilon_{f,Al,1}) - \Gamma_e(\epsilon_{e1})\right] \tag{B9}$$

and for ions

$$I_{Hi,a} = \frac{1}{2} A_a e \left[\Gamma_i(\epsilon_{f,Al,2}) - \Gamma_e(\epsilon_{e2})\right] \tag{B10}$$

Emission of such particles as backscattered and secondary electrons from interior surfaces has been ignored for simplicity. In fact, any such emitted particles are expected either to return to their surface of origin or to strike some other interior surface. The net effect should be to reduce interior potential differences to some extent.

It is now possible to write expressions for the high-energy currents identified in figure 4 and required for the overall current balance. For the forebody surfaces, the exterior and interior high-energy currents are

$$\begin{aligned} I_{He,f} &= -I_{He}\beta + I_{Hi} + I_{BS}\beta + I_{SP} \\ &= \frac{1}{2} A_f e \left\{\left[\Gamma_i(\epsilon_{02}) - \Gamma_i(\epsilon_{f2})\right](1 + \delta_{HP,f}) - \left[\Gamma_e(\epsilon_{01}) - \Gamma_e(\epsilon_{f1})\right](1 - \zeta)\beta\right\} \end{aligned} \tag{B11}$$

$$I_{HEP,a} = I_{Hi,f} - I_{He,f}\beta + I_{Hi,Al} - I_{He,Al}\beta$$

$$= \frac{1}{2} A_f e \left\{ \left[\Gamma_i(\epsilon_{f2}) - \Gamma_i(\epsilon_{f,Al,2}) \right] - \left[\Gamma_e(\epsilon_{f1}) - \Gamma_e(\epsilon_{f,Al,1}) \right] \beta \right.$$

$$\left. + \frac{1}{2} \left[\Gamma_i(\epsilon_{a2}) - \Gamma_i(\epsilon_{e2}) \right] - \frac{1}{2} \left[\Gamma_e(\epsilon_{a1}) - \Gamma_e(\epsilon_{e1}) \right] \beta \right\} \tag{B12}$$

where

$$\delta_{HP,f} = \begin{cases} \delta_p & \text{for } \varphi_f \le 0 \\ \delta_p \exp\left(-\dfrac{e\varphi_f}{kT_S} \right) & \text{for } \varphi_f > 0 \end{cases} \tag{B13a}$$

and

$$\beta = \begin{cases} 1 & \text{for } |\varphi_f| \le \epsilon_{01} \\ \left(1 + \dfrac{e\varphi_f}{\epsilon_{01}} \right) & \text{for } \varphi_f > \epsilon_{01} \\ \exp\left(\dfrac{e\varphi_f}{\epsilon_{01}} \right) & \text{for } \varphi_f < -\epsilon_{01} \end{cases} \tag{B14a}$$

is the factor which accounts for effects of φ_f on high-energy electron collection for large potentials. For the afterbody surface, the exterior and interior high-energy currents are

$$I_{He,a} = \frac{1}{2} A_a e \left\{ \left[\Gamma_i(\epsilon_{02}) - \Gamma_i(\epsilon_{a2}) \right] (1 + \delta_{HP,A}) - \left[\Gamma_e(\epsilon_{01}) - \Gamma_e(\epsilon_{a1}) \right] (1 - \zeta)\gamma \right\} \tag{B15}$$

$$I_{HEP,f} = \frac{1}{2} A_a e \left\{ \left[\Gamma_i(\epsilon_{f,Al,2}) - \Gamma_i(\epsilon_{e2}) \right] - \left[\Gamma_e(\epsilon_{f,Al,1}) - \Gamma_e(\epsilon_{e1}) \right] \gamma \right\} \tag{B16}$$

where $\delta_{HP,a}$ and γ are the equivalents of $\delta_{HP,f}$ and β; that is,

$$\delta_{HP,a} = \begin{cases} \delta_p & \text{for } \varphi_a \leq 0 \\ \delta_p \exp\left(-\dfrac{e\varphi_a}{kT_S}\right) & \text{for } \varphi_a > 0 \end{cases} \tag{B13b}$$

and

$$\gamma = \begin{cases} 1 & \text{for } |\varphi_a| \leq \epsilon_{01} \\ \left(1 + \dfrac{e\varphi_a}{\epsilon_{01}}\right) & \text{for } \varphi_a > \epsilon_{01} \\ \exp\left(\dfrac{e\varphi_a}{\epsilon_{01}}\right) & \text{for } \varphi_a < -\epsilon_{01} \end{cases} \tag{B14b}$$

These equations are summarized in table II.

APPENDIX C

PROBE RESISTANCES AND PENETRATION ENERGIES

Forebody and Afterbody Resistances

Both the forebody and afterbody insulators are composed of different insulating layers, which are treated as resistors in series. The forebody and afterbody resistances R_f and R_a were calculated from bulk resistivities. The thicknesses of the layers were based on information from Ames Research Center personnel and references 6 and 7. Bulk resistivity was based on information from Ames Research Center personnel (carbon-phenolic heat shield) and from measurements made at the Lewis Research Center (fiberglass honeycomb heat shield). The bulk resistivity of Mylar was assumed to be the same as that of Teflon and Kapton, about 10^{17} Ω-cm. The insulated area was taken to be the same as the hemispherical surface area in all cases. The calculation is illustrated in figure 13.

Penetration Energies

The penetration energies are based on Boeing calculations of the probe's structural shielding (fig. 14) and on the range and energy loss tables of Berger and Seltzer (ref. 12) (for electrons) and Barkas and Berger (ref. 13) (for H^+ ions). For the present calculations, the items in figure 14 were grouped into forebody insulators, aluminum structure (including the urethane foam), and afterbody insulators; and penetration energies were calculated by using the range and energy loss tables. Table III summarizes the calculations. For the ions, the calculated energies $\epsilon_{f, Al, 2}$ and ϵ_{e2} are greater than 100 MeV (table III). Because the environmental model cannot predict fluxes for energies above 100 MeV, ion fluxes for $\epsilon_{f, Al, 2} = 100$ MeV were used, and it was assumed that no ions escape the probe completely.

REFERENCES

1. DeForest, Sherman E.: Spacecraft Charging at Synchronous Orbit. J. Geophys. Res., vol. 77, no. 4, Feb. 1, 1972, pp. 651-659.
2. Grard, R. J. L., ed.: Sixth ESLAB Symposium on Photon and Particle Interactions with Surfaces in Space. D. Reidel Publishing Co. (Dordrecht), 1973.
3. Rosen, A., ed.: AIAA/AGU Symposium on Spacecraft Charging by Magnetospheric Plasmas. Progress in Astronautics and Aeronautics Series, vol. 47, MIT Press, 1976.
4. Scarf, F. L.: Plasma Physics Phenomena in the Outer Planet Magnetospheres. AIAA Paper 73-566, July 1973.
5. Jupiter Charged-Particle Environment for Jupiter Orbiter Probe 1981/1982 Mission. JPL 660-24, Jet Propulsion Laboratory, 1976.
6. Outer Planet Atmospheric Entry Probe, System Description. Prepared for the 1975 Committee on Planetary and Lunar Exploration (Complex) Summer Study, Seattle, Washington. Ames Research Center, July 1975.
7. DeFrees, R. E.: Pioneer Jupiter Probe Mission - 1980, Probe Description. (McDonnel Douglas Astronautics Co. - East; NAS 2-8377.) NASA CR-137591, 1974.
8. Whipple, Elden C., Jr.: The Equilibrium Electric Potential of a Body in the Upper Atmosphere and in Interplanetary Space. Ph. D. Thesis, George Washington Univ., 1965.
9. Grard, R. J. L.; Knott, K.; and Pederson, A.: The Influence of Photoelectron and Secondary Electron Emission on Electric Field Measurements in the Magnetosphere and Solar Wind. Sixth ESLAB Symposium on Photon and Particle Interaction with Surfaces in Space, R. J. L. Grard, ed., D. Reidel Publishing Co. (Dordrecht), 1973, pp. 163-189.
10. Willis, R. F.; and Skinner, D. K.: Secondary Electron Emission Yield Behavior of Polymers. Solid State Commun., vol. 13, no. 6, Sept. 15, 1973, pp. 685-688.
11. Purvis, Carolyn K.; Stevens, N. John; and Oglebay, Jon C.: Charging Characteristics of Materials: Comparison of Experimental Results with Simple Analytical Models. NASA TM X-73606, 1976.
12. Berger, Martin J.; and Seltzer, Stephen M.: Tables of Energy Losses and Ranges of Electrons and Positrons. NASA SP-3012, 1964.
13. Barkas, Walter H.; and Berger, Martin J.: Tables of Energy Losses and Ranges of Heavy Charged Particles. NASA SP-3013, 1964.

TABLE I. - THERMAL PLASMA AND PHOTOELECTRON CURRENTS TO PROBE EXTERIOR SURFACES

$$\left[I_{PHO} + I_{TH} = -I_e + I_i + I_s + I_{PHO}\right]$$

(a) Region 1 (in motion)

Probe hemisphere	Potential $\varphi \leq 0$	Potential $\varphi > 0$
	Currents to exterior surfaces	
Forebody	$I_e = j_{eo}A_f \exp\left(\frac{e\varphi_f}{kT_e}\right)$	$I_e = j_{eo}A_f \left(1 + \frac{e\varphi_f}{kT_e}\right)$
	$I_i = 0$	$I_i = 0$
	$I_s = j_{so}A_f \exp\left(\frac{e\varphi_f}{kT_e}\right)$	$I_s = j_{so}A_f \exp\left(-\frac{e\varphi_f}{kT_S}\right)$
	$I_{PHO} = 0$	$I_{PHO} = 0$
Afterbody	$I_e = i_{eo}A_a \exp\left(\frac{e\varphi_a}{kT_e}\right)$	$I_e = j_{eo}A_a \left(1 + \frac{e\varphi_a}{kT_e}\right)$
	$I_i = \pi r_p^2 N_i eV \left(1 - \frac{2e\varphi_a}{M_i V^2}\right)$	$I_i = \pi N_i r_p^2 eV \left(1 - \frac{2e\varphi_a}{M_i V^2}\right)$
	$I_s = j_{so}A_a \exp\left(\frac{e\varphi_a}{kT_e}\right)$	$I_s = j_{so}A_a \exp\left(-\frac{e\varphi_a}{kT_S}\right)$
	$I_{PHO} = 1.8\times10^{-10} A_a$	$I_{PHO} = 1.8\times10^{-10} A_a \exp\left(-\frac{e\varphi_a}{kT_{ph}}\right)$

(b) Region 2 (at rest)

Probe hemisphere	Potential $\varphi \leq 0$	Potential $\varphi > 0$
	Currents to exterior surfaces	
Forebody	$I_e = j_{eo}A_f \exp\left(\frac{e\varphi_f}{kT_e}\right)$	$I_e = j_{eo}A_f \left(1 + \frac{e\varphi_f}{kT_e}\right)$
	$I_i = j_{io}A_f \left(1 - \frac{e\varphi_f}{kT_i}\right)$	$I_i = j_{io}A_f \exp\left(-\frac{e\varphi_f}{kT_i}\right)$
	$I_s = j_{so}A_f \exp\left(\frac{e\varphi_f}{kT_e}\right)$	$I_s = j_{so}A_f \exp\left(-\frac{e\varphi_f}{kT_S}\right)$
	$I_{PHO} = 0$	$I_{PHO} = 0$
Afterbody	$I_e = j_{eo}A_a \exp\left(\frac{e\varphi_a}{kT_e}\right)$	$I_e = j_{eo}A_a \left(1 + \frac{e\varphi_a}{kT_e}\right)$
	$I_i = j_{io}A_a \left(1 - \frac{e\varphi_a}{kT_i}\right)$	$I_i = j_{io}A_a \exp\left(-\frac{e\varphi_a}{kT_i}\right)$
	$I_s = j_{so}A_a \exp\left(\frac{e\varphi_a}{kT_e}\right)$	$I_s = j_{so}A_a \exp\left(-\frac{e\varphi_a}{kT_S}\right)$
	$I_{PHO} = 1.8\times10^{-10} A_a$	$I_{PHO} = 1.8\times10^{-10} A_a \exp\left(-\frac{e\varphi_a}{kT_{ph}}\right)$

TABLE II. - HIGH-ENERGY-PARTICLE CURRENTS TO PROBE INTERIOR AND EXTERIOR SURFACES

(a) Exterior

Probe hemisphere	Currents to exterior surfaces
Forebody, $I_{He,f} = -I_{He}{}^{\beta} + I_{Hi} + I_{BS}{}^{\beta} + I_{SP}$	$I_{He} = \frac{1}{2} A_f e \left[\Gamma_e(\epsilon_{01}) - \Gamma_e(\epsilon_{f1})\right]$ $I_{Hi} = \frac{1}{2} A_f e \left[\Gamma_i(\epsilon_{02}) - \Gamma_i(\epsilon_{f2})\right]$ $I_{BS} = \zeta I_{He}$ $I_{SP} = \delta_{HP,F} I_{Hi}$
Afterbody, $I_{He,a} = -I_{He}{}^{\gamma} + I_{Hi} + I_{BS}{}^{\gamma} + I_{SP}$	$I_{He} = \frac{1}{2} A_a e \left[\Gamma_e(\epsilon_{01}) - \Gamma_e(\epsilon_{a1})\right]$ $I_{Hi} = \frac{1}{2} A_a e \left[\Gamma_i(\epsilon_{02}) - \Gamma_i(\epsilon_{a2})\right]$ $I_{BS} = \zeta I_{He}$ $I_{SP} = \delta_{HP,A} I_{Hi}$

(b) Interior

Probe hemisphere	Currents to interior surfaces
Forebody, $I_{HEP,a} = I_{Hi,f} - I_{He,f}{}^{\beta} + I_{Hi,Al} - I_{He,Al}{}^{\beta}$	$I_{Hi,f} = \frac{1}{2} A_f e \left[\Gamma_i(\epsilon_{f2}) - \Gamma_i(\epsilon_{f,Al,2})\right]$ $I_{He,f} = \frac{1}{2} A_f e \left[\Gamma_e(\epsilon_{f1}) - \Gamma_e(\epsilon_{f,Al,1})\right]$ $I_{Hi,Al} = \frac{1}{4} A_f e \left[\Gamma_i(\epsilon_{a2}) - \Gamma_i(\epsilon_{e2})\right]$ $I_{He,Al} = \frac{1}{4} A_f e \left[\Gamma_e(\epsilon_{a1}) - \Gamma_e(\epsilon_{e1})\right]$
Afterbody, $I_{HEP,f} = -I_{He,a}{}^{\gamma} + I_{Hi,a}$	$I_{He,a} = \frac{1}{2} A_a e \left[\Gamma_e(\epsilon_{f,Al,1}) - \Gamma_e(\epsilon_{e1})\right]$ $I_{Hi,a} = \frac{1}{2} A_a e \left[\Gamma_i(\epsilon_{f,Al,2}) - \Gamma_i(\epsilon_{e2})\right]$

TABLE III. - PROBE DEPENDENT PARAMETERS USED

Parameter	Symbol	Value	Basis
Forebody surface area	A_f	1.27 m^2	r_p = 0.45 m (refs. 6,7)
Afterbody surface area	A_a	1.27 m^2	r_p = 0.45 m
Maximum secondary-electron yield (electron impact)	δ_m	4.8	Ref. 11
Energy to attain δ_m	ϵ_m	175 eV	Ref. 11
Backscattering coefficient	ζ	0.05	Estimated (ref. 11)
Secondary emission-electron yield coefficient (ion impact)	δ_p	1	Estimated (ref. 8)
Temperature of emitted secondary electrons	kT_S	2 eV	Ref. 8
Temperature of emitted photoelectrons	kT_{ph}	2 eV	Ref. 9
Resistance of forebody insulators	R_f	$4.09\times10^{11}\Omega$	Estimated (appendix C)
Resistance of afterbody insulators	R_a	$3.25\times10^{11}\Omega$	Estimated (appendix C)
Lowest high energy:			
For electrons	ϵ_{01}	0.06 MeV	----------
For ions	ϵ_{02}	1 MeV	----------
Energy to penetrate forebody insulators:			
For electrons	ϵ_{f1}	15.1 MeV	Estimated (appendix C)
For ions	ϵ_{f2}	99.5 MeV	
Energy to penetrate forebody insulators and aluminum structure:			
For electrons	$\epsilon_{f,Al,1}$	16.5 MeV	
For ions	$\epsilon_{f,Al,2}$	[a]123.6 MeV	
Energy to penetrate afterbody insulators:			
For electrons	ϵ_{a1}	0.7 MeV	
For ions	ϵ_{a2}	24.4 MeV	
Energy to pass through probe:			
For electrons	ϵ_{e1}	17.2 MeV	
For ions	ϵ_{e2}	[a]148 MeV	

[a]100 MeV; model is good only to 100 MeV; $\epsilon_{f,Al,2}$ = 100 MeV and $\epsilon_{e2} > 100$ MeV used (θ flux).

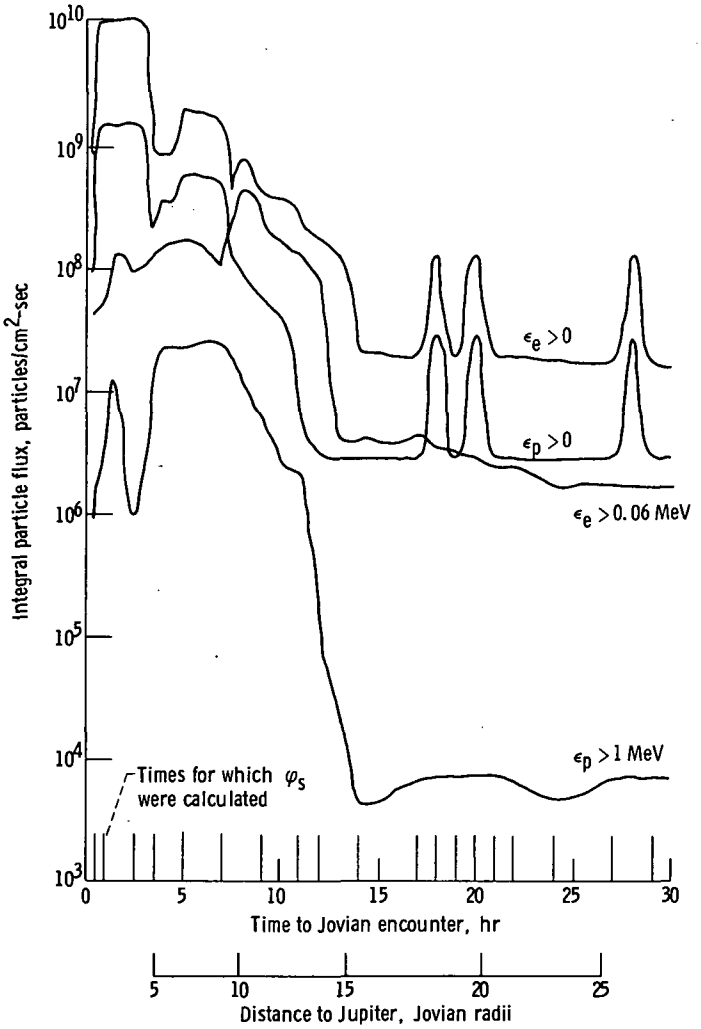

Figure 1. - Jovian particle fluxes along probe trajectory.

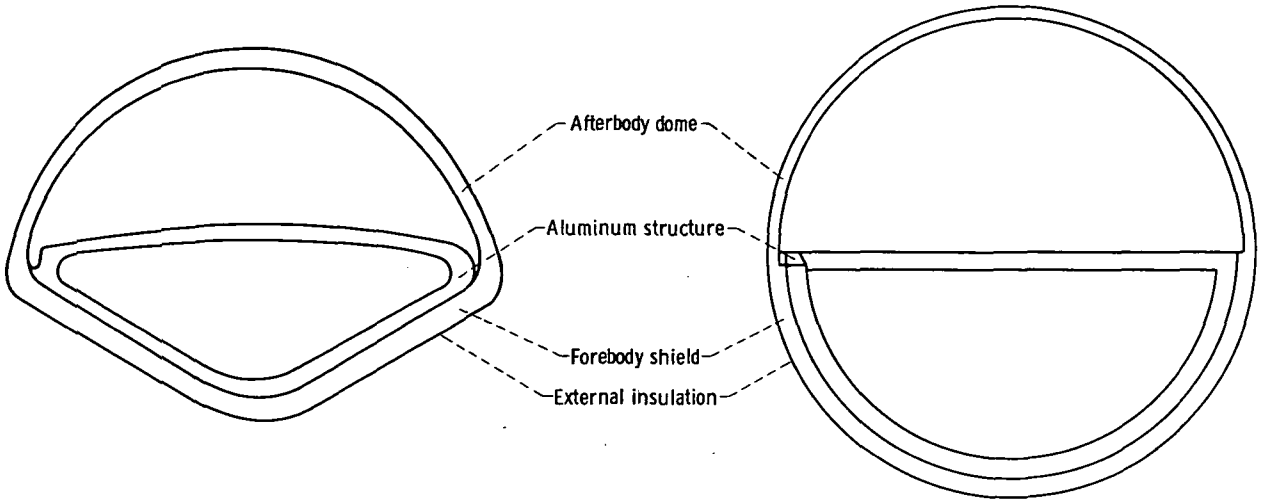

(a) Actual probe configuration.

(b) Spherical probe model.

Figure 2. - Probe and model geometries.

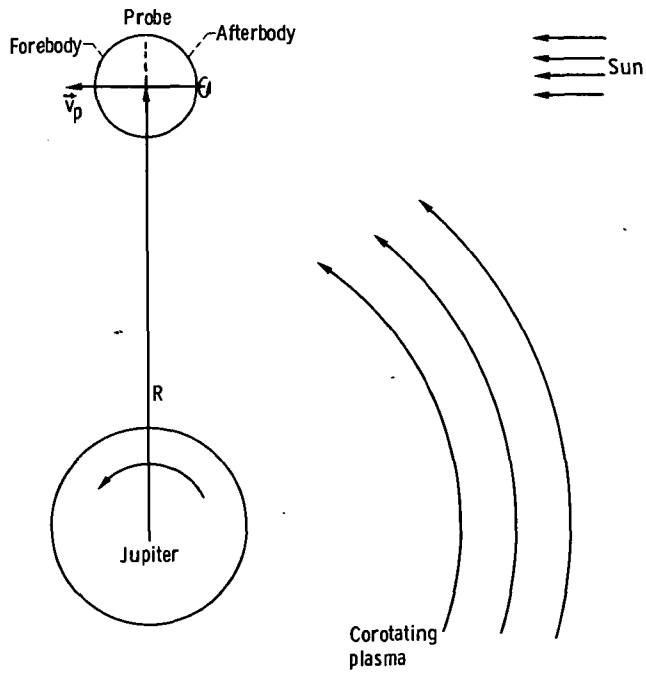

Figure 3. - Assumed geometry.

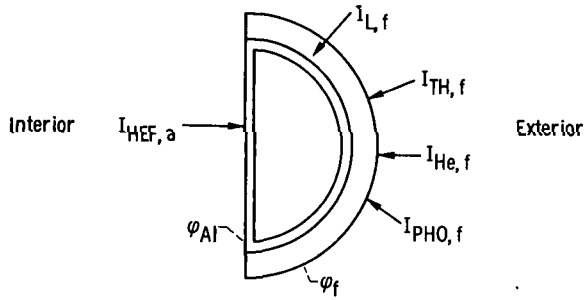

(a) Forebody.

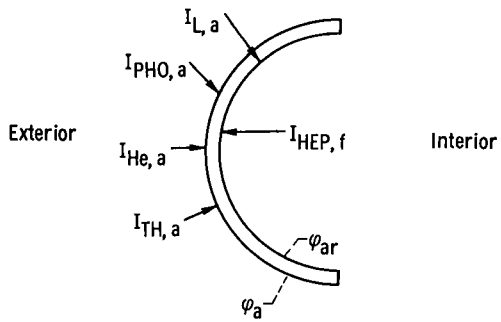

(b) Afterbody.

Source of current	Symbol for -	
	Forebody	Afterbody
High-energy fluxes on exterior	$I_{He,f}$	$I_{He,a}$
Thermal plasma	$I_{TH,f}$	$I_{TH,a}$
Photoemission	$I_{PHO,f}$	$I_{PHO,a}$
High-energy fluxes penetrating to interior	$I_{HEP,a}$	$I_{HEP,f}$
Leakage through insulators	$I_{L,f}$	$I_{L,a}$

Figure 4. - Definition of model currents.

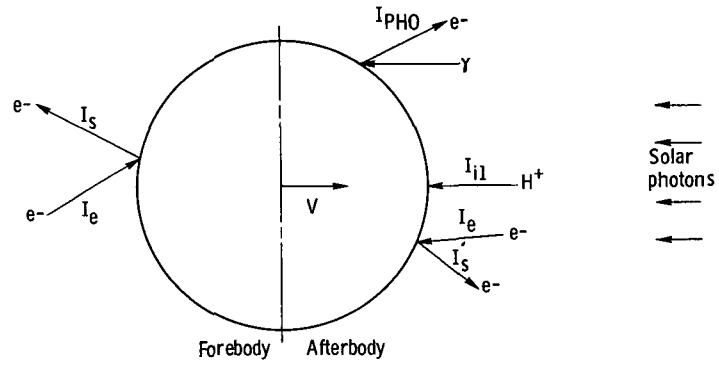

(a) Region 1: probe in motion.

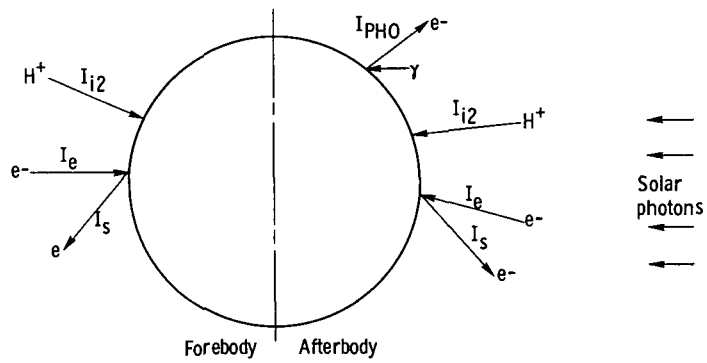

(b) Region 2: probe at rest.

Figure 5. - Thermal and photoelectron currents to probe.

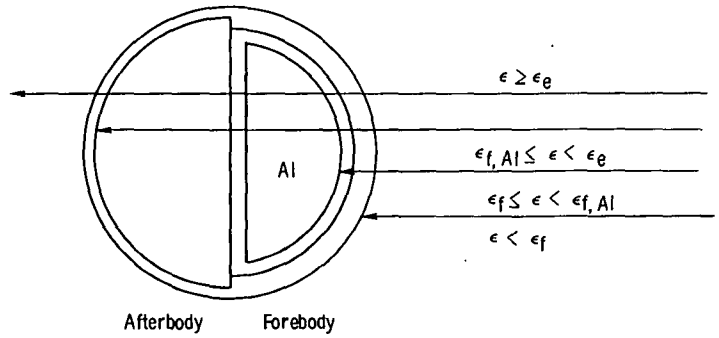

(a) From forward direction.

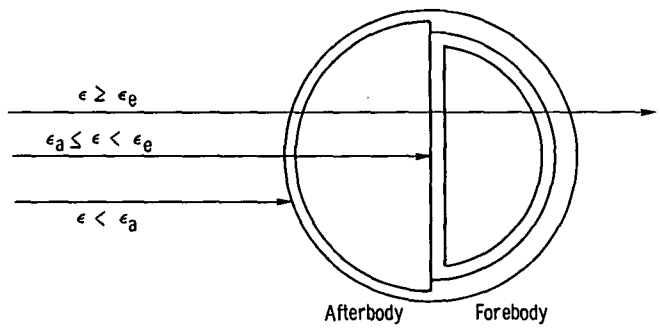

(b) From aft direction.

Figure 6. - High-energy particles impinging on probe, where ϵ_f is the energy to completely penetrate forebody insulators; $\epsilon_{f,Al}$ is the energy to completely penetrate both forebody insulators and aluminum structure; ϵ_e is the energy to penetrate entire probe and escape; and ϵ_a is the energy to completely penetrate afterbody insulators.

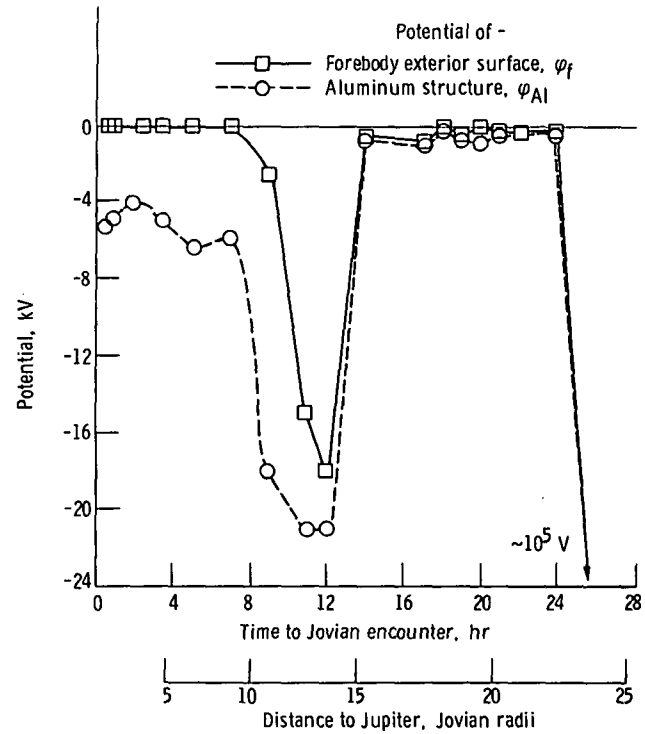

Figure 7. - Potentials attained by probe forebody.

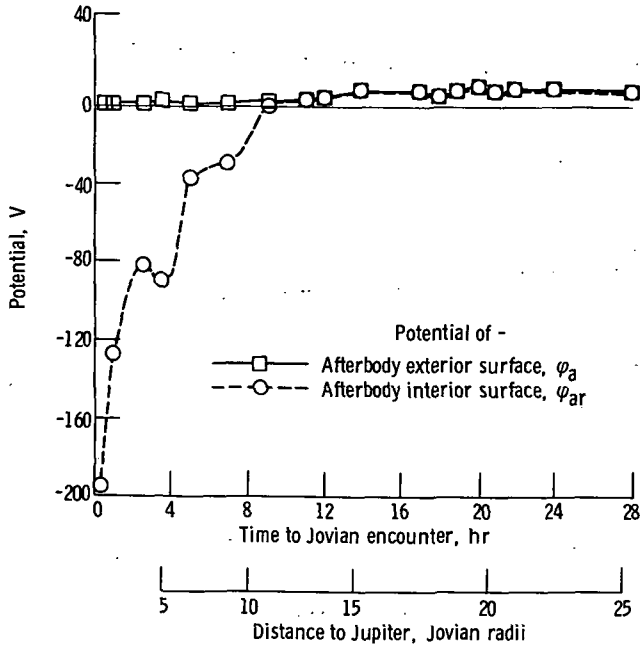

Figure 8. - Potentials attained by probe afterbody.

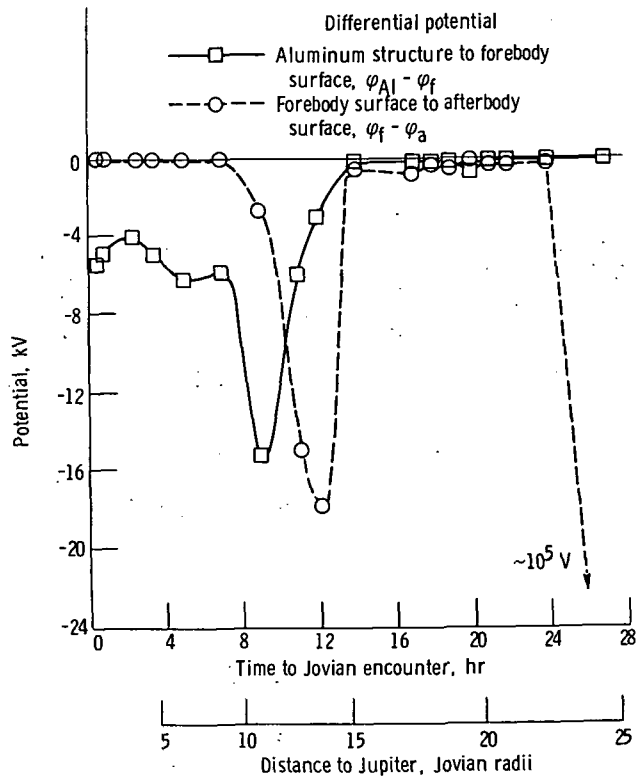

Figure 9. - Differential potentials.

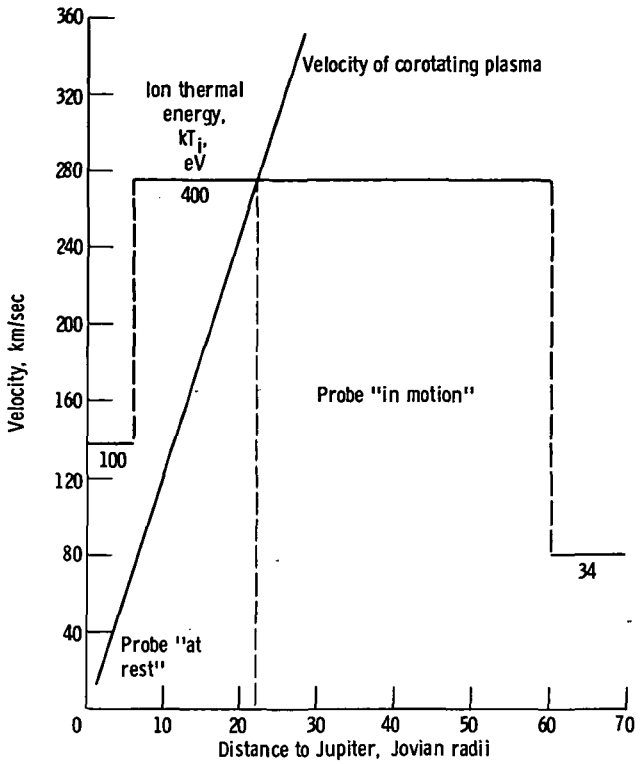

Figure 10. - Ion thermal and plasma corotation velocities.

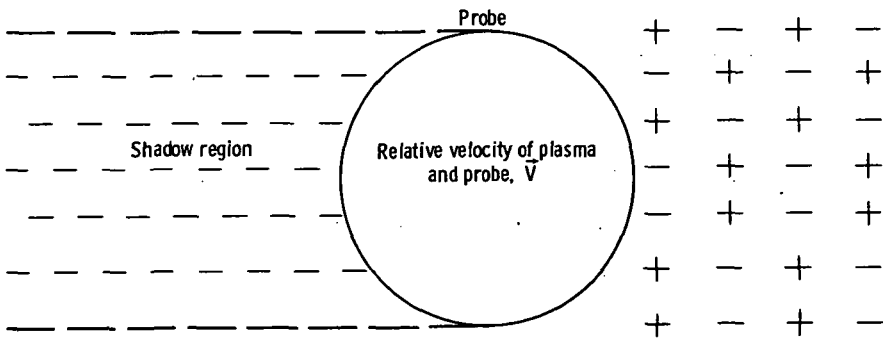

Figure 11. - Corotation effect on ion collection. (Ions are assumed to be collected on only the "front" surface of the probe when $|\bar{V}|$ is greater than the ion random thermal velocity.)

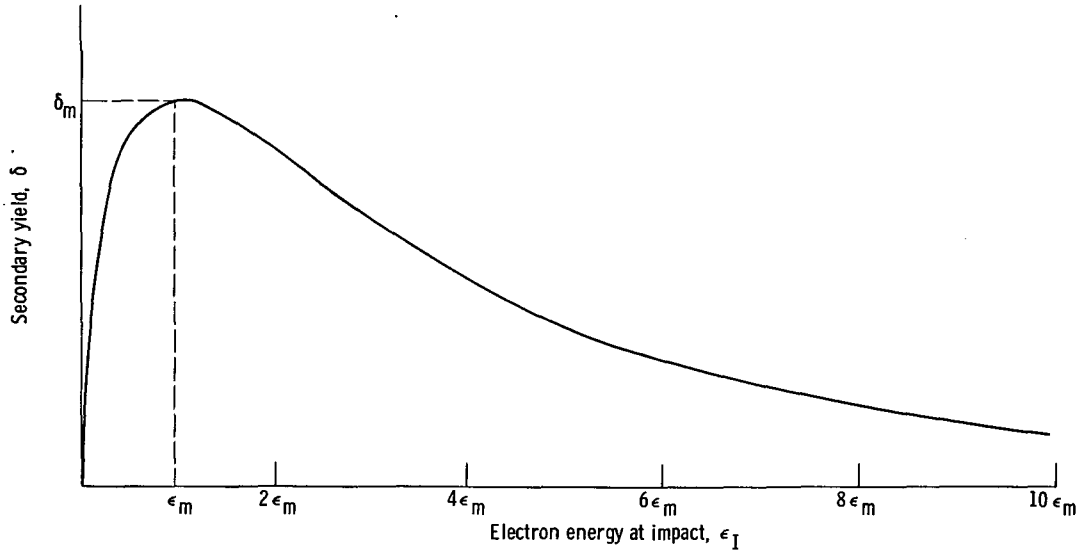

Figure 12. - Secondary electrons released by electron impact, where $\delta_{\epsilon_I} = 7.4\,\delta_m \frac{\epsilon_I}{\epsilon_m} \exp\left(-2\sqrt{\frac{\epsilon_I}{\epsilon_m}}\right)$. (For Mylar, $\delta_m = 4.8$; $\epsilon_m = 175$ eV.)

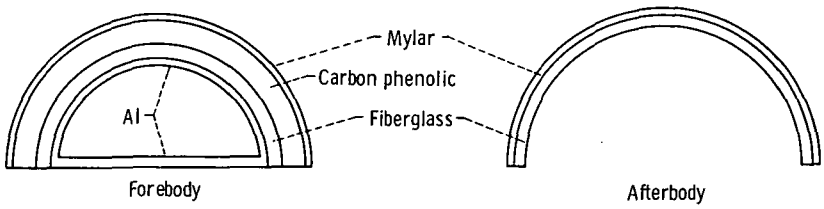

$R = \rho l/A$ in Ω, where $A = 1.27 \times 10^4$ cm2

Material	Forebody			Afterbody		
	Resistivity, ρ, Ω-cm	Thickness, l, cm	Resistance, R, Ω	Resistivity, ρ, Ω-cm	Thickness, l, cm	Resistance, R, Ω
Mylar	10^{17}	0.029	2.3×10^{11}	10^{17}	0.029	2.3×10^{11}
Carbon phenolic	2×10^5	9.33	147	----	-----	--------
Fiberglass	10^{15}	2.28	1.79×10^{11}	10^{15}	1.2	9.5×10^{10}
			4.09×10^{11}			3.25×10^{11}

Figure 13. - Calculation of forebody and afterbody resistances.

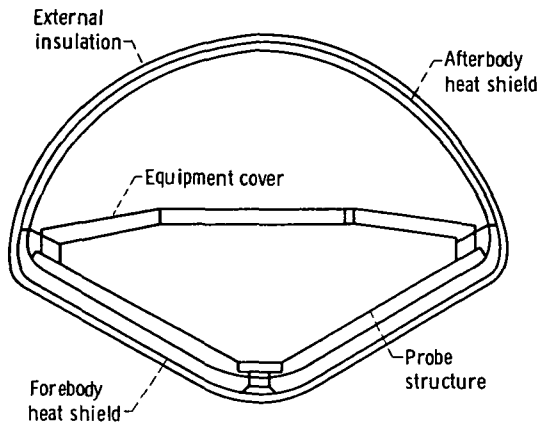

Section	Shielding	Material	Density, g/cm^2
Forebody	Exterior insulation	Multilayer Mylar	0.11
	Forebody heat shield	Carbon phenolic	7.75
	Heat shield backup	Fiberglass honeycomb	.05
	Structure	Aluminum	.42
			8.33
Equipment cover	Interior insulation	Urethane foam	0.16
	Structure	Aluminum	.22
			0.38
Afterbody	Exterior insulation	Multilayer Mylar	0.11
	Heat shield	Fiberglass honeycomb	.49
			0.60

Figure 14. - Probe structural shielding.

1. Report No. NASA TP-1263	2. Government Accession No.	3. Recipient's Catalog No.
4. Title and Subtitle JUPITER PROBE CHARGING STUDY		5. Report Date January 1979 6. Performing Organization Code
7. Author(s) Carolyn K. Purvis		8. Performing Organization Report No. E-9167 10. Work Unit No. 506-23
9. Performing Organization Name and Address National Aeronautics and Space Administration Lewis Research Center Cleveland, Ohio 44135		11. Contract or Grant No. 13. Type of Report and Period Covered Technical Paper
12. Sponsoring Agency Name and Address National Aeronautics and Space Administration Washington, D.C. 20546		14. Sponsoring Agency Code

15. Supplementary Notes

This study was performed in conjunction with the Jupiter Probe Program at the NASA Ames Research Center.

16. Abstract

A model to predict spacecraft charging effects in the Jovian magnetosphere was developed for the preliminary design of a Jupiter probe. Charging calculations made with this model are presented and discussed. Differential potentials between interior and exterior surfaces and between sunlit and dark exterior surfaces are predicted to be in the kilovolt range.

17. Key Words (Suggested by Author(s))	18. Distribution Statement
Spacecraft charging Jupiter probe Spacecraft design	Unclassified - unlimited STAR Category 18

19. Security Classif. (of this report)	20. Security Classif. (of this page)	21. No. of Pages	22. Price*
Unclassified	Unclassified	36	A03

* For sale by the National Technical Information Service, Springfield, Virginia 22161

NASA-Langley, 1979

National Aeronautics and
Space Administration

Washington, D.C.
20546

Official Business
Penalty for Private Use, $300

THIRD-CLASS BULK RATE

Postage and Fees Paid
National Aeronautics and
Space Administration
NASA-451

NASA

POSTMASTER: If Undeliverable (Section 158
Postal Manual) Do Not Return